LANGMUIR Article
Cite This: Langmuir 2017, 33, 10838-10850
pubs.acs.org/Langmuir

Thermocapillary Droplet Actuation: Effect of Solid Structure and Wettability

George Karapetsas, Nikolaos T. Chamakos, and Athanasios G. Papathanasiou*

School of Chemical Engineering, National Technical University of Athens, Athens 15780, Greece

Supporting Information

ABSTRACT: We examine the thermocapillary-driven flow of a droplet on a nonuniformly heated patterned surface. Using a sharp-interface scheme, capable of efficiently modeling the flow over complex surfaces, we perform 2D and 3D finite element simulations for a wide range of substrate wettabilities, i.e., from hydrophilic to superhydrophobic surfaces. Our results demonstrate that the contact angle hysteresis, due to the presence of the solid structures, is responsible for the appearance of a critical thermal gradient beyond which droplet migration is possible; the latter has been reported by experimental observations. The migration velocity as well as the direction of motion strongly depend on the combined action of the net mechanical force along the contact line and the thermocapillary induced flow at the liquid−air interface. We also show that through proper control and design of the substrate wettability, contact angle hysteresis, and induced flow field it is possible to manipulate the droplet dynamics: in particular, controlling its motion along a predefined track or entrapping by a wetting defect a droplet based on its size, as well as providing appropriate conditions for enhanced mixing inside the droplet.

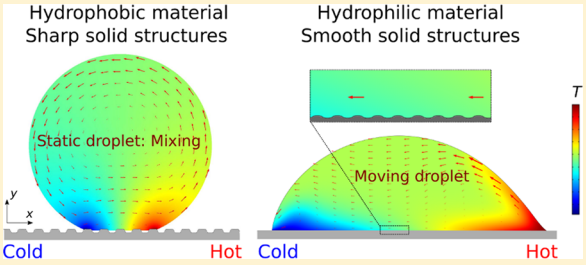

1. INDRODUCTION

The application of a body force or external gradient can be used as a mechanism for the actuation of liquid droplets, and the ability to control these properties can play a key role in many technological applications that involve microfluidics.[1−3] Lately, a range of microfluidic devices based on the thermocapillary effect have been proposed and developed for different purposes such as actuation, sensing, trapping, sorting, mixing, chemical reaction, and biological assays.[4]

Thermocapillary actuation is typically induced by the presence of a temperature gradient along the substrate which causes a temperature gradient along the interface giving rise to surface tension gradients. The latter induce Marangoni stresses which drive liquid flow from warmer to colder regions. In practice, however, the substrates encountered are never completely flat or perfectly smooth, exhibiting finite roughness or even well-defined features in the form of stripes or pillars. The scope of the present work is to provide a model and investigate the thermocapillary droplet actuation on patterned solid substrates.

Early experimental work by Bouasse[5] has shown that the thermocapillary effect can be used to force a drop to climb a tilted wire, against gravity, by heating its lower end; the drop moves toward the cold region of the wire. Similar experiments have been conducted by Yarin et al.[6] using various liquids on glass fibers and copper wires, whereas other research groups have conducted experiments on horizontal smooth or rough surfaces to investigate systematically the migration of thin liquid drops.[7−10]

More specifically, Brzoska et al.[7] performed experiments using polydimethylsiloxane (PDMS) oil drops on silanized silicon flat surfaces and showed that it was possible to get a steady migration of droplets with a fixed shape toward the cold region, while for a temperature gradient below a certain threshold, the drop may not move due to the effect of contact angle hysteresis. These findings were also confirmed by more recent studies.[8,10] Pratap et al.,[9] on the other hand, performed experiments using decane drops on PDMS-coated substrates and showed that in their case there was a significant dependence of the contact angle on temperature, which was demonstrated by the significant distortion of the footprint of the drop from a circular shape. In contrast to previous experiments the migration velocity was shown to decrease as the drop moves toward colder regions, and this was attributed to either the presence of a temperature dependent viscosity or the effect of evaporation, which was non-negligible.[9] It has been suggested recently though that the decrease of the migration velocity could also be due to some extent to the dependence of the contact angle on temperature due to the change of material wettability as the slender drop moves toward colder regions.[11]

The thermocapillary droplet migration has been the subject of several theoretical studies in the literature, which were mainly conducted under the thin film approximation. Brochard[12] examined the motion of droplets in the presence of chemical or thermal gradients, assuming a thin-edge shape of

Received: August 7, 2017
Revised: September 22, 2017
Published: September 22, 2017

DOI: 10.1021/acs.langmuir.7b02762
Langmuir 2017, 33, 10838−10850

the drop while employing force balance and energy arguments to deduce the wetting characteristics in terms of the spreading coefficient. The work of Brochard[12] was generalized by Ford and Nadim[13] to allow for arbitrary shapes of the drop and also allowed the contact angles to be different at the two ends, and later on by Pratap et al.[9] who extended this theory to three-dimensional drops.

Smith[14] was able to derive evolution equations for the droplet height which were solved numerically to derive quasi-steady solutions in the presence of thermal gradients. To this end, he employed a dynamic boundary condition at the contact line, which relates the velocity of the contact line to the dynamic contact angle, also taking into account the effect of contact angle hysteresis. According to his analysis, only two possible steady states exist: either a motionless drop or a steady migration of the droplet with a fixed shape toward colder regions. Very recently, though, Gomba and Homsy[15] revisited this problem using lubrication theory in combination with a precursor model to relieve the contact line singularity and they identified three different regimes with increasing wettability of the solid surface which range from a droplet regime to a transitional regime with rather complex dynamics involving breakup of the drop into smaller droplets, and a film regime. Karapetsas et al.[11] considered the variation of contact angle with temperature along the solid surface, and observed rich droplet dynamics including a stick−slip behavior. Later on, Karapetsas et al.[16] examined the effect of a non-monotonic dependence of surface tension on temperature, a typical characteristic of self-rewetting fluids, and found under certain conditions the existence of very high spreading rates. In a slightly different context, the effect of thermal Marangoni stresses on droplets attached on a heated solid substrate has also been studied by Ehrhard and Davis[17] who employed lubrication theory to describe the spreading of a droplet on a uniformely heated plate, and Anderson and Davis[18] who also took into account the effect of evaporation. The latter effect was also studied recently by Karapetsas et al.,[19] while Chen et al.[20] studied the phenomenon of thermocapillary nonwetting.

The case of a droplet with large contact angles was not examined until very recently by Sui.[21] Earlier efforts in this direction were also done by Tseng et al.,[22] the model of which lacks sufficient detail and does not obtain agreement with experiments, and by Nguyen and Chen[23] who apparently neglected the surface tension gradient term from the interfacial stress balance equation, significantly affecting their results since Marangoni is the driving force for this flow. Sui[21] employed the level-set method and considered droplets with large contact angles also taking into account the viscous effects of the fluid outside the droplet. Interestingly, it was shown that the direction of migration depends on the wettability of the solid surface. For small contact angles the droplet migrates toward the cold side, whereas for large contact angles the droplet migrates toward the hot region, and for intermediate contact angles the droplet may even fall in a motionless state. As shown, the direction of motion is also affected by the viscosity ratio between the droplet and the ambient fluid. These results have been confirmed and extended to 3D drops by Fath and Bothe.[24] Additionally, the flow field inside a stationary water droplet on a hydrophobic surface was recently visualized by Pradhan and Panigrahi.[25]

All of the aforementioned theoretical studies consider substrates that are macroscopically smooth. Experimental observations, though, seem to indicate that the presence of patterned solid surfaces may affect significantly the migration of liquid droplets. Recently, Dai et al.[10] investigated the influence of surface roughness and surface topography orientation and it was shown that the orientation of grinding scars may guide the direction of movement of drops. On the other hand, experiments on surfaces with microdimples suggest that the morphology of the substrate can be used for inhibiting thermocapillary migration. To the best of our knowledge, the effect of the substrate topography has not been addressed theoretically in the literature, and this will be the main objective of this paper. To this end, we use a recently proposed sharp-interface scheme which treats the liquid−gas and the liquid−solid interfaces in a unified context (one equation for both interfaces) by introducing a Lennard-Jones type of potential to model the microscale liquid−solid interactions.[26−29]

This model has been shown to be particularly efficient in the case of patterned surfaces since its main advantage is that it avoids the implementation of an explicit boundary condition at the contact line and there is no requirement for the predefinition of the number and position of the contact lines. As will be shown below, our model favorably compares against other works in the literature and can be used for a wide range of wettabilities, i.e., from hydrophilic to superhydrophobic surfaces. It is also demonstrated that the presence of surface structure gives rise to a finite static contact angle hysteresis which is responsible for the fact that droplet migration becomes possible beyond a critical thermal gradient. Moreover, we examine how this effect can be exploited to manipulate droplets (e.g., sorting, passive control of motion direction) or to produce efficient micromixers.

The remainder of the paper is organized as follows. In Section 2, we describe the system of governing equations and outline the numerical scheme that is used for the simulations. The results are presented and discussed in Section 3. Finally, the concluding remarks are given in Section 4.

2. PROBLEM FORMULATION

We consider the dynamics of a drop of an incompressible, nonvolatile Newtonian fluid with constant density ρ, viscosity, μ, specific heat capacity C_p, and thermal conductivity λ, which has been deposited on a rigid and impermeable patterned solid substrate subjected to a constant temperature gradient (see Figure 1). In the most general case that will be examined in the present work, we consider that the wall temperature is given by

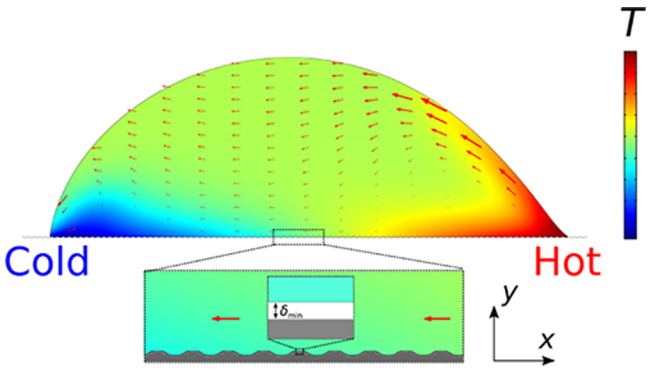

Figure 1. Schematic of a droplet sliding on a patterned solid substrate inclined under the influence of an applied temperature gradient. The origin of the coordinate system is placed atop the solid surface and at the position of the center of mass of the droplet at $t = 0$.

DOI: 10.1021/acs.langmuir.7b02762
Langmuir 2017, 33, 10838−10850

$T_w = T_o + \gamma(x \cos \alpha - z \sin \alpha)$, where α denotes the angle of the temperature gradient with respect to the x-axis along the xz-plane. In the limiting case of a 2D droplet shown in Figure 1, we assume $\alpha = 0$ and thus T_w is simply given by $T_w = T_o + \gamma x$. T_o denotes the temperature of the solid surface at $(x,z) = (0,0)$; we assume that this is the position on the solid surface of the center of mass of the droplet at $t = 0$. We assume that the droplet has a nominal radius, R, which is defined as $R = \sqrt{A/\pi}$ for the case of 2D droplets with surface area, A, and as $R = \sqrt[3]{3V/4\pi}$ for axisymmetric or in general 3D droplets with volume, V. The surface tension of the liquid−gas interface is denoted with σ and is assumed to vary linearly with temperature, $\sigma = \sigma_o - \psi(T - T_o)$; $\psi = -(\mathrm{d}\sigma/\mathrm{d}T)$.

We render the governing equations dimensionless by scaling all lengths with the nominal droplet radius, R. Since a characteristic velocity is not known a priori, we choose the following scaling for the velocity field, $V^* = \sqrt{\sigma_o/\rho R}$. The pressure is scaled with σ_o/R and the stresses with $\mu V^*/R$. Finally, time is scaled with R/V^*. Substituting this scaling into the governing equations and boundary conditions, the dimensionless groups that emerge are the Ohnesorge number, $\mathrm{Oh} = \mu/\sqrt{\rho\sigma_o R}$, the Marangoni number, $\mathrm{Ma} = \psi T_o/\sigma_o$ and the dimensionless thermal gradient $\Gamma = \gamma R/T_o$.

The spreading dynamics is governed by the equations of the conservation of mass, momentum and energy, given below:

$$\frac{\partial \mathbf{v}}{\partial t} + \mathbf{v}\cdot\nabla\mathbf{v} + \nabla P - \mathrm{Oh}\nabla^2\mathbf{v} = 0 \tag{1}$$

$$\nabla\cdot\mathbf{v}_i = 0 \tag{2}$$

$$\frac{\mathrm{Pr}}{\mathrm{Oh}}\left(\frac{\partial T}{\partial t} + \mathbf{v}\cdot\nabla T\right) - \nabla^2 T = 0 \tag{3}$$

where ∇ denotes the gradient operator and $\mathbf{v}$ is the velocity vector. Here, P denotes the pressure and I is the identity tensor. In the present study the effect of gravity has been neglected since we are mainly interested in the case of small sized droplets.

2.1. Boundary Conditions. The solution of the above set of equations is determined subject to the following boundary conditions. Following the approach of Chamakos et al.[28] we treat the gas and solid phases in a unified context. Along the liquid−air or liquid−solid interface the flow field satisfies the local interfacial force balance between the stresses in the liquid and the ambient phase

$$\mathbf{n}\cdot\tau = \mathbf{n}\cdot\tau_{\mathrm{ext}} + \mathrm{Oh}^{-1}(2\mathcal{H}\sigma\mathbf{n} + \nabla_s\sigma) \tag{4}$$

where $\mathbf{n}$ denotes the outward unit normal, τ is the total stress tensor

$$\tau = -PI + (\nabla\mathbf{v} + \nabla\mathbf{v}^T) \tag{5}$$

τ_{ext} denotes the total stress tensor of the ambient phase and $2\mathcal{H}$ is the mean curvature of the interface

$$2\mathcal{H} = -\nabla_s\cdot\mathbf{n} \tag{6}$$

while ∇_s is the surface gradient operator, defined as

$$\nabla_s = (I - \mathbf{nn})\nabla \tag{7}$$

The dimensionless surface tension is given by

$$\sigma = 1 - \mathrm{Ma}(T - 1) \tag{8}$$

Taking the tangential and normal to the free surface components of this force balance, we obtain

$$\mathbf{n}\cdot\tau\cdot\mathbf{n} = \mathbf{n}\cdot\tau_{\mathrm{ext}}\cdot\mathbf{n} + \frac{2\mathcal{H}}{\mathrm{Oh}} \tag{9}$$

$$\mathbf{n}\cdot\tau\cdot\mathbf{t} = \mathbf{n}\cdot\tau_{ext}\cdot\mathbf{t} + \frac{1}{\mathrm{Oh}}\nabla_s\sigma\cdot\mathbf{t} \tag{10}$$

where $\mathbf{n}\cdot\tau_{\mathrm{ext}}\cdot\mathbf{n}$ and $\mathbf{n}\cdot\tau_{\mathrm{ext}}\cdot\mathbf{t}$ denote the normal and tangential stress component of the ambient phase, respectively. Assuming that the viscosity in the gas phase is negligible, the effect of the flow in the gas can be neglected. Moreover, following the approach of refs 28 and 29 we introduce the normal microscale liquid−solid interactions through a disjoining pressure term, Π, which accounts for the presence of antagonistic short- and long-range intermolecular forces

$$\mathbf{n}\cdot\tau_{\mathrm{ext}}\cdot\mathbf{n} = -P_g + \Pi \tag{11}$$

where

$$\Pi = \frac{w_{ls}}{\mathrm{Oh}}\left[\left(\frac{A}{\delta + \epsilon}\right)^{C_1} - \left(\frac{A}{\delta + \epsilon}\right)^{C_2}\right] \tag{12}$$

The wetting parameter, w_{ls}, is directly related with the substrate wettability through the following relation

$$\cos\theta_Y = \frac{w_{ls}(C_1 - C_2)A}{(C_1 - 1)(C_2 - 1)} - 1 \tag{13}$$

where θ_Y denotes the Young's equilibrium contact angle and the exponents C_1 and C_2 control the range of the microscale liquid−solid interactions; large values of C_1 and C_2 reduce the range within which microscale interactions are active. In eq 12, δ denotes the euclidean distance of separation between the solid and the liquid surface. The minimum distance of separation, δ_{min} (see Figure 1), between the liquid and solid phases is controlled by the constants A and ϵ, i.e., $\delta_{\mathrm{min}} = A - \epsilon$; ϵ is a regularization parameter and typically acquires very small values.

In order to account for the tangential stresses $\mathbf{n}\cdot\tau_{\mathrm{ext}}\cdot\mathbf{t}$, that the liquid experiences along the liquid−solid interface, we employ the approach of Karapetsas et al.[29] by introducing the Navier slip model

$$\mathbf{n}\cdot T_{\mathrm{ext}}\cdot\mathbf{t} = \beta_{\mathrm{eff}}(\mathbf{t}\cdot\mathbf{v}) \tag{14}$$

where β_{eff} denotes the effective slip length or slip coefficient. Since our formulation treats the gas and solid phases in a unified context, a continuous function is needed, and to this end, we employ the following expression

$$\beta_{\mathrm{eff}} = \beta_{sl}\left(1 - \tanh\left[\alpha\left(\frac{\delta}{\delta_{\mathrm{min}}} - 1\right)\right]\right) \tag{15}$$

β_{sl} is a parameter which accounts for the adhesion properties of the liquid droplet on the solid surface. According to eq 15 β_{eff} is equal to β_{sl} along the liquid−solid interface (for $\delta \approx \delta_{\mathrm{min}}$) and zero everywhere else, implying a shear-free boundary condition along the liquid−gas interface; this variation is controlled by the parameter α and takes place at a smaller length scale than the action of the disjoining pressure. If β_{sl} acquires very large values we recover the usual no-slip boundary condition along the liquid−solid interface, whereas for moderate values of this parameter partial slip is allowed.[29]

DOI: 10.1021/acs.langmuir.7b02762
Langmuir 2017, 33, 10838−10850

Finally, we apply along the interface the following generalized boundary condition for the temperature field

$$\mathbf{n}\cdot\nabla T = -h_{\text{eff}}(T - T_w) \tag{16}$$

where h_{eff} is an efficient dimensionless heat transfer coefficient and is given, similarly to β_{eff}, by a continuous function

$$h_{\text{eff}} = h_w\left(1 - \tanh\left[\alpha\left(\frac{\delta}{\delta_{\min}} - 1\right)\right]\right) \tag{17}$$

According to eq 17, h_{eff} becomes equal to h_w along the liquid−solid interface (for $\delta \approx \delta_{\min}$) and zero everywhere else, implying a no-flux boundary condition along the liquid−gas interface. Assuming that the parameter h_w acquires large values, along the liquid−solid interface we recover the usual continuity boundary condition, i.e., $T \approx T_w$.

Along the moving interface we impose the kinematic boundary condition

$$(\mathbf{v} - \mathbf{v}_{\text{mesh}})\cdot\mathbf{n} = 0 \tag{18}$$

where $\mathbf{v}_{\text{mesh}}$ is the velocity of the mesh at the interface. Finally, to complete our model we have to set a datum pressure, and as such, we impose the pressure in the gas phase to be equal to zero $P_g = 0$, without loss of generality.

2.2. Model of the Substrate Topography. As noted above, for the purposes of this study we will consider the cases of both a macroscopically flat and a structured solid surface. The model for the former case is quite straightforward and has been described above. For the case of a patterned solid surface we will follow two alternative routes.

2.2.1. Explicit Model for Geometrical Pattern. The first approach is to explicitly consider the topography of the solid surface (see Figure 1), and this is taken into account by describing the roughness of the solid using analytical expressions (see eqs 22 and 23). In this case special consideration is required on the definition of distance, δ, in eq 12. Obviously, in the limiting case of a macroscopically flat substrate, δ can be simply taken to be equal to the vertical distance from the solid surface. On the other hand, in the case of a surface with geometric structures of finite size, we follow the approach of Chamakos et al.[26−28] taking δ to be equal to the minimum distance from the solid which is obtained by solving the eikonal equation.[30] As discussed in Chamakos et al.[26] this choice gives the best agreement with mesoscale simulations of wetting on structured surfaces, though, with considerably lower computational demands. This approach will mainly be used for the 2D simulations presented below.

2.2.2. Emulation of Substrate Pattern with Chemical Heterogeneity. Despite the efficiency of the explicit method described above, the computational cost becomes significantly high when it comes to the study of droplets on surfaces with 3D patterns. Karapetsas et al.[29] proposed an alternative route and applied their method to the study of droplets in "fakir" state, where the presence of air pockets within the roughness may act as effective "shear free" regions. According to this approach, we may assume that the substrate is macroscopically flat and the effect of heterogeneity due to the presence of patterns is introduced simply by taking the wettability, adhesion, and heat transfer properties along the solid surface to be a function of the substrate coordinates (i.e., a case similar to that considering chemical heterogeneity). The method that will be described below will be used for the 3D simulations presented below where we will focus on the case of droplets attached to composite hydrophobic surfaces, with patterns of different wettabilities, e.g., stripes of a microstructured surface.

When dealing with a heterogeneous hydrophobic surface with intrinsic wettability, θ_Y, a simple way to take into account how the apparent contact angle, θ_a, changes due to the presence of small air pockets in the material roughness is to consider the Cassie−Baxter equation

$$\cos(\theta_a) = \omega\cos(\theta_Y) + \omega - 1 \tag{19}$$

where ω is the fraction of solid surface area wet by the liquid. It is reasonable to assume that the presence of air pockets also affects the wall slip and heat transfer coefficients by decreasing their values, and this is taken into account by considering the following dependence on ω

$$\beta'_{sl} = \omega\beta_{sl} \quad \text{and} \quad h'_w = \omega h_w \tag{20}$$

Finally to model the presence of a composite substrate, we assume that the value of ω varies in the spatial coordinates (x, z) and this is modeled by solving the following equation

$$\nabla^2\omega(x, z) = 0 \tag{21}$$

subject to the following conditions: to indicate at a certain position the presence of a microstructured stripe (with apparent contact angle $\theta_a = \theta_{a,1}$) we impose ω to be equal to $\omega = [\cos(\theta_{a,1}) + 1]/[\cos(\theta_Y) + 1)]$, while we set $\omega = 1$ for a regular part of the surface (without microstructures), i.e., with apparent contact angle $\theta_{a,2} = \theta_Y$.

Using this method, it is possible to emulate the presence of a structured solid surface with significantly reduced computational cost. In Figure 2, we depict examples of patterns which may exhibit large scale structures either in the form of pillars (Figure 2a) or in the form of stripes (Figure 2b). The red color depicts the parts of the solid surface which correspond to the part of the hydrophobic surface with similar properties to the intrinsic properties of the surface (i.e., $\omega = 1$, $\theta_{a,2} = \theta_Y = 120°$) whereas the blue color depicts the parts of the solid surface which correspond to $\theta_{a,1} = 150°$ and $\omega = 0.268$. The difference in the structure of these two cases significantly affects the overall apparent contact angle of the droplet which in the case of Figure 2a is ∼142°, whereas in the case of Figure 2b is ∼135°, as well as the eventual coverage of the solid surface by the liquid droplet; the outer circle in both figures depicts the footprint of an unstructured surface with $\theta_Y = 120°$.

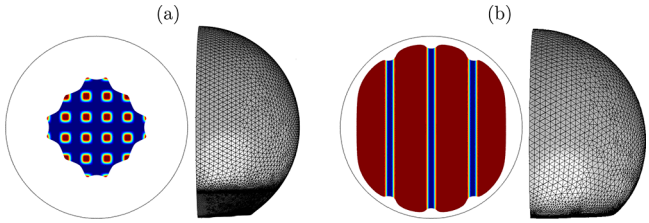

Figure 2. Footprint and sideview of a static droplet that rests on a solid surface modeled with eq 21: (a) surface with pillars and (b) surface with stripes. The red color depicts the parts of the solid surface with $\theta_{a,2} = \theta_Y = 120°$ and the blue color with $\theta_{a,1} = 150°$. The outer circle depicts the footprint of an unstructured surface with $\theta_Y = 120°$.

2.3. Numerical Implementation. The above set of equations is combined with an elliptic grid generation scheme capable of following the deformations of the physical domain.[28,19] In order to adequately resolve the flow, the mesh is refined around the moving liquid−air or liquid−solid

DOI: 10.1021/acs.langmuir.7b02762
Langmuir 2017, 33, 10838−10850

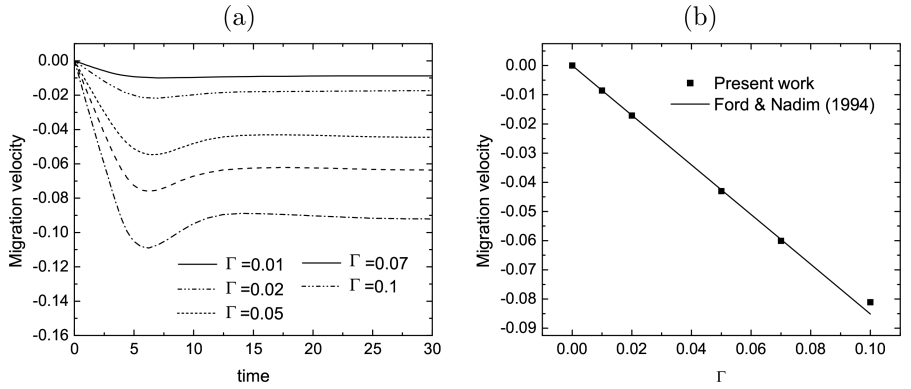

Figure 3. (a) Evolution of the migration velocity with time for various values of Γ. (b) Steady migration velocity as a function of Γ and comparison with theoretical predictions by Ford and Nadim.[13] Oh = 0.07, Pr = 10, Ma = 0.5, θ_Y = 30°, α = 0°.

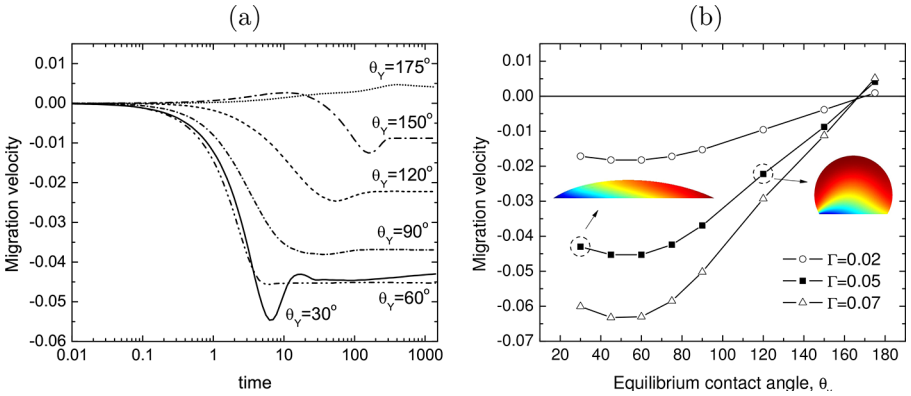

Figure 4. (a) Evolution of the migration velocity with time for various values of θ_Y for Γ = 0.05. (b) Steady migration velocity as a function of θ_Y for various values of Γ; the insets depict the steady profile of the droplet on a hydrophilic and a hydrophobic surface along with contour plots of the corresponding temperature field. Oh = 0.07, Pr = 10, Ma = 0.5, α = 0°.

interface. For all the computations presented in this paper, numerical checks have shown that the results converge with mesh refinement. The set of algebraic equations is integrated in time with the implicit Euler method. The model has been implemented in COMSOL Multiphysics commercial software.

3. RESULTS

For the simulations that will be presented below we consider the disjoining pressure constants values in accordance with previous studies,[27−29] namely: C_1 = 12, C_2 = 10, A = 0.009, ϵ = 0.008, unless noted otherwise.

3.1. Smooth Solid Surface—Model Validation. In this section, we present numerical results of a droplet moving on a smooth solid surface under the influence of a thermal gradient. In Figure 3a we demonstrate the temporal evolution of the droplet's migration velocity for various thermal gradient, Γ, values. It is observed that the migration velocity reaches a peak absolute value just after the droplet starts to move ($t \approx 5$). Soon after that ($t \geqslant 25$), when a steady shape has been reached, the droplet exhibits a virtually constant migration velocity (terminal or steady velocity). In order to validate our model, here we compare the computed terminal velocities (for various Γ values) with the ones predicted from the theoretical model of Ford and Nadim.[13] In the latter approach, the steady state value of the droplet's migration velocity is predicted by equating the mechanical force, due to the surface tension difference, at the three-phase contact line and the shear force on the wall, computed with lubrication approximation. Moreover, Ford and Nadim have considered a fixed droplet shape with a relatively large, width to height, aspect ratio (i.e., for hydrophilic substrates). In Figure 3b we plot the terminal migration velocity computed by the proposed model (black line), as well as the theoretical predictions by Ford and Nadim (black squares). As shown, without any other fitting, the proposed model is able to capture the theoretical predictions. It is important to note here that we do not make any simplifications regarding the droplet shape in our model. It is worth noting that in addition to the work of Ford and Nadim, our formulation can also predict the behavior of a droplet far from the lubrication limit (e.g., for hydrophobic substrates), as will be shown below.

The temporal evolution of the droplet's migration velocity, for different wettabilities and for Γ = 0.05, is depicted in Figure 4a. Once again, it is shown that after exhibiting some fluctuations in the migration velocity, finally a steady shape, with a constant velocity, is reached. An overall picture of the solid wettability effect on the droplet motion can be obtained by plotting, in Figure 4b, the terminal migration velocity (when a steady droplet shape has been reached) as a function of θ_Y, for various thermal gradient values. It is interesting to observe here that the steady migration velocity of the droplet has a nonmonotonic dependence on the Young contact angle, θ_Y, value. Specifically, our simulations suggest that there is a maximum migration speed, which appears at $\theta_Y \approx 50°$, in line with the predictions made by Sui.[21] In addition, as shown, the migration velocity then reduces with the Young contact angle

DOI: 10.1021/acs.langmuir.7b02762
Langmuir 2017, 33, 10838−10850

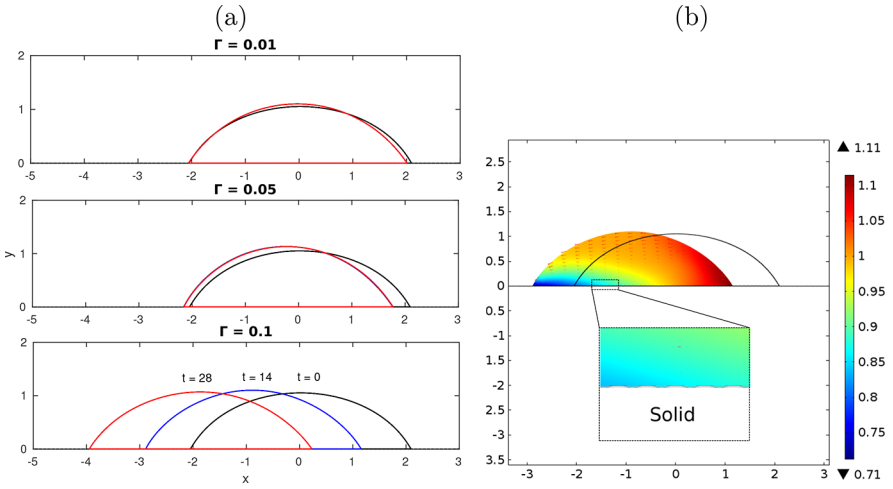

Figure 5. Rough surface: (a) Droplet profiles at t = 0, 14, 28 for various values of Γ. (b) Contour plot of the temperature field at t = 14 and for Γ = 0.1. Oh = 0.07, Pr = 10, Ma = 0.5, θ_Y = 60°, α = 0°.

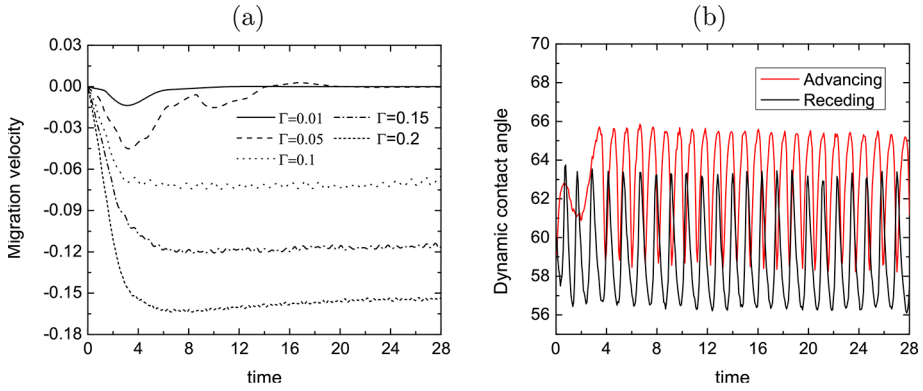

Figure 6. Rough surface: Evolution of (a) the migration velocity with time for various values of Γ and (b) advancing and receding contact angles for Γ = 0.1. Oh = 0.07, Pr = 10, Ma = 0.5, θ_Y = 60°, α = 0°.

increment (i.e., when reducing the material wettability). Interestingly, it is found that below a specific wettability threshold (for $\theta_Y \approx 165°$), the droplet moves to the opposite direction (toward the hot region). The two different motion regimes (toward and against the cold region) are separated by the black horizontal line which corresponds to a motionless case.

These results are in line with the simulations that have been presented by Sui[21] who employed the level-set method taking into account also the viscous effects of the fluid outside the droplet. As discussed by Sui, the direction of motion is decided by the combined action of the mechanical force at the two contact lines and the thermocapillary flow that is induced along the interface. The latter always drives the droplet toward the colder regions whereas the action of the former depends on the wettability (toward colder and hotter regions for hydrophilic and hydrophobic surfaces, respectively). The simulations performed by Sui suggested that with decreasing viscosity ratios (i.e., ambient fluid becoming less viscous) the critical value of contact angle for motionless state increases, since the viscous resistance mitigates the effect of the thermocapillary flow, and eventually reaches an asymptote at approximately 100°. Our simulations, however, indicate that in the case of an ambient fluid with negligible viscosity the critical contact angle arises at approximately 165°. The difference with the findings of Sui[21] could be due to the known inefficiency of the level-set method to handle flows with very large or small viscosity and density ratios resulting in a reduced accuracy. The above does not stand for our sharp-interface scheme.

3.2. Geometrically Structured Solid Surface.

3.2.1. Stripes with Smooth Edges and Shallow Undulations. In this section, we proceed with our simulations for a droplet migrating on a geometrically structured solid surface. The topography of the solid surface, in this case, is given by the following analytical expression:

$$h(x) = p_1 \sin(p_2 x) \tag{22}$$

where the parameters p_1 and p_2 regulate the width and height of the protrusions, respectively. We select a case with rather shallow structures in order to create a surface that macroscopically looks smooth. In particular, by setting p_1 = 0.001 and p_2 = 78.537, we obtain a unit structure height of 0.001 and width of 0.08. Considering a characteristic length, R = 1 mm (nominal radius of the droplet), the above correspond to a height of 1 μm and width of 80 μm, respectively. The equilibrium (Young's) contact angle in this case is set to 60°, where, as shown in Figure 4b, the droplet's migration velocity is close to its maximum value.

According to our previous work,[29] the surface roughness can significantly affect the flow dynamics (inducing contact angle hysteresis) even if the solid structures are shallow. In particular, in an analogy to the gravity-driven droplet motion on an

DOI: 10.1021/acs.langmuir.7b02762
Langmuir 2017, 33, 10838−10850

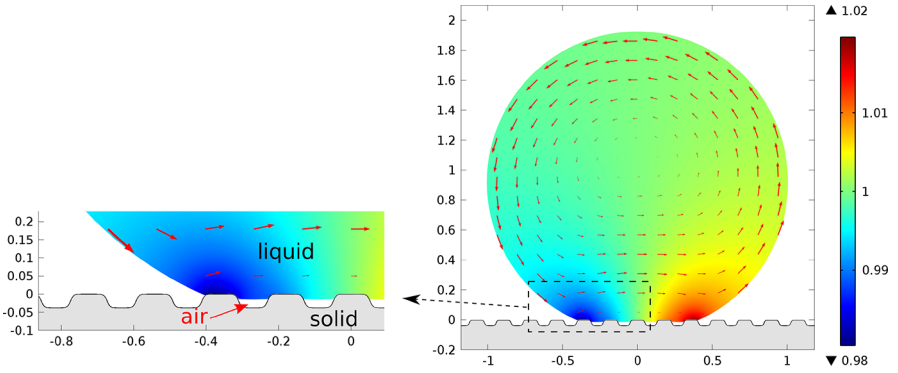

Figure 7. Contour plots of the temperature field, T, at t = 17647, for a droplet on a structured substrate with p = 0.04, w = 0.1, d = 0.08, and s = 0.008. The liquid velocity field is presented with the arrow lines. The remaining parameters are Γ = 0.05, Oh = 0.24, Pr = 1, Ma = 0.136, α = 0°.

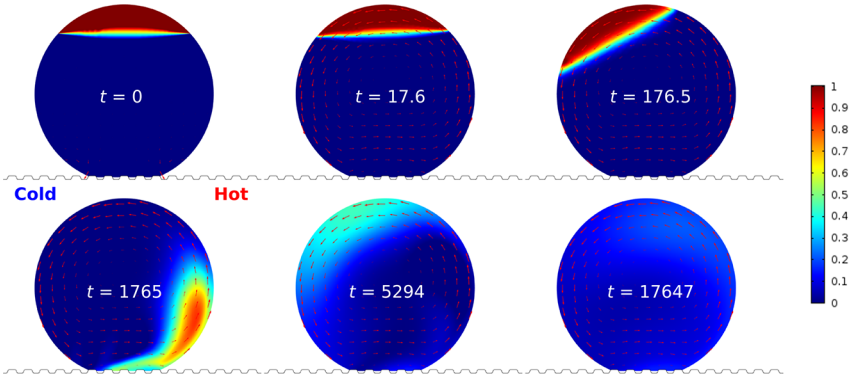

Figure 8. Contour plots of the dye concentration, c, at t = 0, 17.6, 176.5, 1765, 5294, and 17647, for a droplet on a structured substrate under the influence of a temperature gradient along the solid surface; the direction of the temperature gradient is indicated in the panel for t = 0 and remains constant throughout the simulation. The liquid velocity is presented with the arrow lines. Pe = 1.76 × 10^5, Γ = 0.05, Oh = 0.24, Pr = 1, Ma = 0.136, α = 0°.

inclined substrate, presented in ref 29, it would be expected that the droplet will not move unless the static hysteresis (the limiting hysteresis in which the droplet can remain at a standstill) has been surpassed. Such an argument is shown in Figure 5a, where the droplet profiles at t = 0, 14, 28 for various values of Γ are plotted. Initially, for Γ = 0.01, the droplet just rearranges from its equilibrium shape and then reaches a new equilibrium state. Specifically, the rear part of the droplet slightly moves whereas the front part remains pinned. Clearly, the model predicts the effect of static hysteresis, unlike the case of a macroscopically flat substrate where no static hysteresis is predicted. By increasing the thermal gradient (Γ = 0.05), we observe that both the rear and the front parts of the droplet have been displaced; however, the droplet soon reaches a new equilibrium state and remains stationary thereafter. Finally, by further increasing Γ to the value of 0.1, the droplet starts to move along the structured substrate and acquires a constant average velocity. The contour plot of the temperature field in this case, at t = 14, is demonstrated in Figure 5b. It is important to note here that in the thermocapillary-driven flow, the rear part of the droplet is first set in motion, contrary to the gravity-driven droplet in ref 29.

In Figure 6a we demonstrate the temporal evolution of the migration velocity for various values of Γ. As also discussed previously, the droplet starts to migrate after a thermal gradient limit ($\Gamma \approx 0.05$) is surpassed. Thereafter, the droplet's speed increases monotonically with Γ. Predicting the dynamic contact angle hysteresis is also of great importance for applications (note that an amount of roughness is always present even in the molecularly smooth surfaces due to the discrete nature of the lattice structure of solids[31]). In particular, in Figure 6b we present the evolution of the dynamic advancing and receding contact angles. We observe that the dynamic contact angles exhibit an oscillatory behavior as the droplet moves on the solid asperities. The average dynamic contact angle hysteresis in this case is found to be approximately equal to 3.9° (where the average advancing and receding contact angles are 62.9° and 59°, respectively).

3.2.2. Sharp Stripes. At this point we turn our attention to deeper structures which may allow the presence of air pockets between the drop and the solid surface. This situation is often encountered in superhydrophobic surfaces (e.g., the lotus leaf[32]), for which the effective heat transfer coefficients and wettability properties attract significant scientific interest in a variety of applications. There is only a limited number of papers that deal with thermocapillary phenomena on such surfaces,[33] since the droplet, in this case, is almost spherical and hence not amenable to lubrication approximations. Here, we will consider a solid structure which is described by the following expression:

$$h(x) = \frac{p}{2}\left[\tanh\left(\frac{x - (d + w/2)}{s}\right) - \tanh\left(\frac{x - w/2}{s}\right)\right] \quad (23)$$

where w and d denote the width of troughs and crests, respectively, p denotes the height of the protrusions, and s is a regularization parameter.

DOI: 10.1021/acs.langmuir.7b02762
Langmuir 2017, 33, 10838−10850

According to our previous analysis (see Figure 4), it would be expected, due to the emerging high apparent contact angle ($\theta_a \approx 154°$, for $p = 0.04$, $w = 0.1$, $d = 0.08$, and $s = 0.008$), that the droplet would fall into a motionless state in this case. In particular, in Figure 7 the droplet shape at $t = 17647$ is practically identical to the initial state ($t = 0$). Despite the absence of net movement, however, we observe a single rotating vortex which covers the entire volume of the droplet (see Figure 7) which is clearly due to the effect of the thermocapillary induced flow along the liquid−air interface. The contour plot in Figure 7 depicts the temperature field, and as shown, liquid is driven from the hot to the cold area along the interface due to the effect of the induced Marangoni stresses. It should be noted that such flow patterns have been reported in the recent experimental work by Pradhan and Panigrahi.[25] An interesting application of such a system is the rapid mixing of reagents (used, e.g., in chemical reactions) in microfluidic devices.[34] Efficient mixing is one of the key challenges in such miniaturized devices since the flow patterns are usually laminar (turbulent mixing is prevented due to the small size of microfluidic devices).[35,36] The quality of mixing is thus very important parameter and is investigated in the following section.

3.3. Droplet as Micromixer. We initially consider a droplet, on a structured solid surface, which is partially stained with dye (see Figure 8 at $t = 0$). The diffusion and convection of dye is then described by the following transport equation:

$$\mathrm{Pe}\left(\frac{\partial c}{\partial t} + \mathbf{v}\cdot\nabla c\right) - \nabla^2 c = 0 \tag{24}$$

where c is the dimensionless dye concentration and $\mathrm{Pe} = V^* R/D_i$ is the Péclet number, with D_i the diffusivity of the dye. In Figure 8 we present the mixing patterns (dye concentration) for various time instances. We observe that the droplet has finally homogenized (at $t = 17647$), concluding that such a technique could prove useful to force a droplet mixing in microfluidic applications.

The effect of dye diffusivity (embodied in the Péclet number) and the thermal gradient, Γ, on the quality of mixing are quantified in Figure 9 at a specific time instance ($t = 17647$). In particular, we adopted the criterion that we denote the droplet as mixed when the maximum concentration value, c_{max}, has dropped to 25% of its initial value (the initial dye concentration value is 1 in the stained region, as observed in Figure 8). In Figure 9 we observe two distinct regions corresponding to mixed (blue circles) and unmixed (red squares) droplets. In addition, the mixing quality is enhanced by increasing the thermal gradient. The considerably short mixing time observed here renders the thermocapillary effect as an efficient method between the existing alternatives (e.g., with electrowetting-induced droplet oscillations[37,38] or with flow through a serpentine channel[39,40]). Specifically, by considering a thermal gradient of 6 °C mm, for a droplet with, e.g., nominal radius $R = 1 \times 10^{-3}$ m, viscosity $\mu = 6 \times 10^{-2}$ Pa s, and $\mathrm{Pe} = 1.76 \times 10^4$, we observe that a complete mixing has been obtained at $t \approx 20$ s. This is comparable with using electrowetting to oscillate the droplet (the latter requires approximately 50 s for the specific liquid viscosity).[37,38]

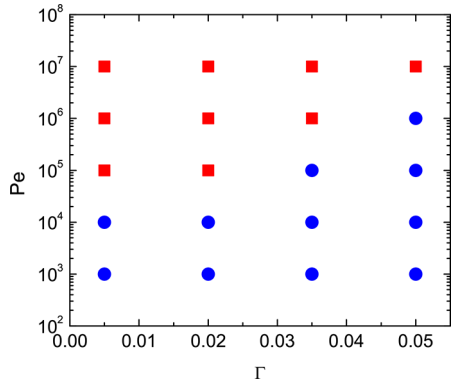

Figure 9. Flow map with mixed (blue circles) and unmixed (red squares) droplets for various values of the Pe number and Γ. We consider that the droplet has been mixed when the maximum dye concentration value, c_{max}, has dropped at least to 25% of its initial value, at $t = 17647$. Oh = 0.24, Pr = 1, Ma = 0.136, $\alpha = 0°$.

In order to quantify the degree of mixing, we analyze, in Figure 10a, the evolution of the maximum concentration of dye, c_{max}, in time for Γ = 0.05. The Péclet number ranges from 1.76×10^3 (green circles) to 1.76×10^6 (magenta circles). It is interesting here that the time required for achieving mixing increases logarithmically with the Péclet number, as observed in Figure 10b. Such a result is similar to the values obtained by Stroock et al.[39] and by Mugele et al.[38] for chaotic mixing in microchannels and in electrowetting-induced droplet oscillations, respectively. The above indicates that a chaotic advection-based mixing regime[41] can be achieved as a result of the thermal Marangoni stresses.

3.4. 3D Droplet on Patterned Substrate. So far we have examined the simplified case of a 2D droplet. It should be noted though that the flow inside a droplet due to the presence the thermal gradient, which sets a preferred direction on the flow, the structure of the solid surface and the geometrical restriction of the droplet shape renders the nature of this problem inherently three-dimensional and the study of the 3D characteristics of the flow can be important for realistic cases. To address this problem we have also performed full 3D simulations which will be presented in this section.

Here we will focus on two different setups. First we will consider the case of solid that exhibits a striped surface and we will investigate how the orientation of the temperature gradient with respect that of the stripes may affect the characteristics of the flow as well as the droplet droplet motion. Next, we will consider the case of smooth and uniform solid surface that exhibits a perforated superhydrophobic defect (see Figure 14a) and we will examine under which conditions the droplet may be driven through this defect. It should be noted that the 3D simulations are computationally demanding and for these simulations we use different values for the disjoining pressure constants ($C_1 = 8$, $C_2 = 6$, $A = 0.038$) since it is easier to be resolved with coarser grids (the local curvature at the contact line attains smaller values) without overly affecting the solution accuracy (see also ref 29).

3.4.1. Orientation of the Temperature Gradient with Respect to a Striped Surface. In this section we investigate the effect of the surface topography and how it may influence the migration behavior of droplets. As noted above, Dai et al.[10] have recently investigated experimentally the influence of surface topography orientation and it was shown that the relative orientation of the surface structures may guide the moving direction of drops or under conditions may also act as a barrier impeding drop movement along the temperature gradient.

DOI: 10.1021/acs.langmuir.7b02762
Langmuir 2017, 33, 10838−10850

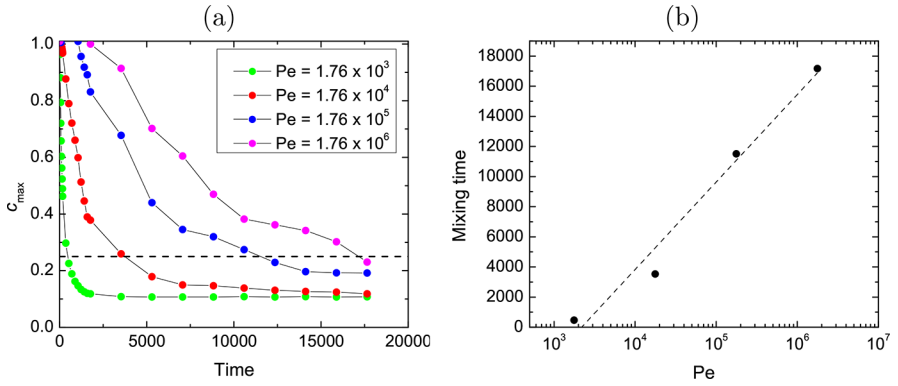

Figure 10. (a) Maximum concentration of dye, c_{max}, vs time, for $\Gamma = 0.05$ and various Péclet numbers. The dashed line ($c_{max} = 0.25$) defines the threshold level used to indicate mixing. (b) Logarithmic dependence of the mixing time on the Péclet number ($\Gamma = 0.05$). The remaining parameters are Oh = 0.24, Pr = 1, Ma = 0.136, $\alpha = 0°$.

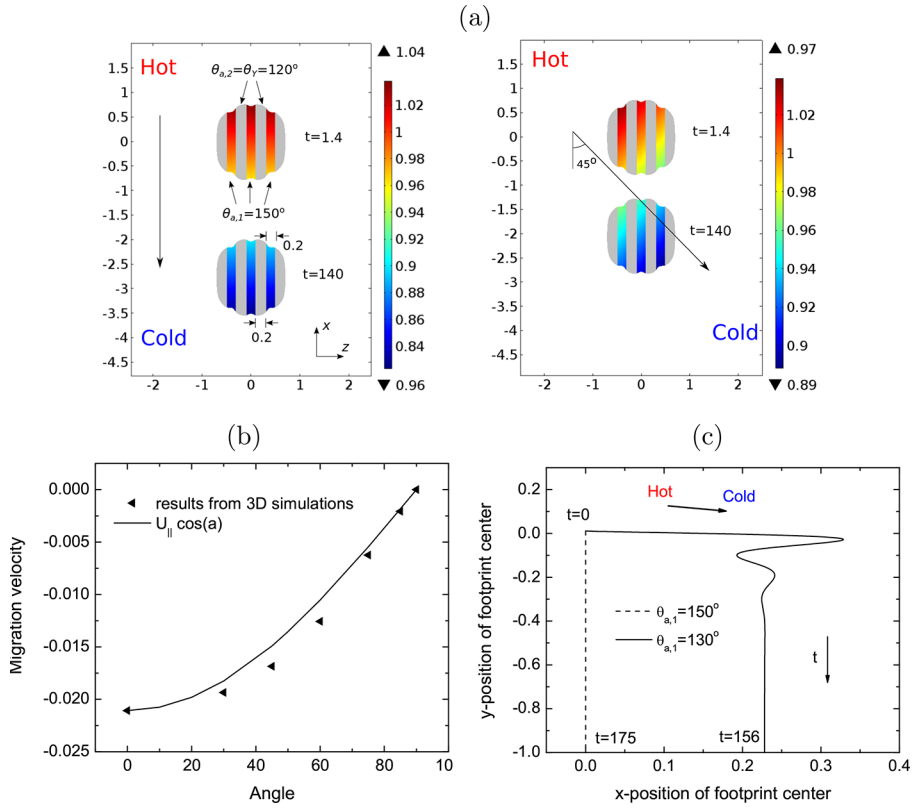

Figure 11. (a) Temperature profiles and positions of the droplet footprint at $t = 1.4$, 140, for a temperature gradient along the solid surface that is in parallel ($\alpha = 0°$) and at an angle $\alpha = 45°$ with the direction of the stripes of the solid surface. (b) Steady migration velocity as a function of the thermal gradient angle and comparison with a theoretical curve assuming that the migration velocity is given by $U_{||} \cos \alpha$. (c) Spatiotemporal evolution of the footprint center of the droplet for a temperature gradient at an angle $\alpha = 75°$ with hydrophobic stripes of $\theta_{a,1} = 130°$ (see movie S1) and $\theta_{a,1} = 150°$; in both cases $\theta_{a,2} = \theta_Y = 120°$. The remaining parameters are Oh = 0.07, Pr = 10, Ma = 0.5, $\Gamma = 0.05$, $\theta_Y = 120°$.

In a similar setup with Dai et al.,[10] we consider a droplet that rests on a striped surface and we apply a temperature gradient at a varying angle with respect to the stripes; in our case the solid is considered to be hydrophobic, $\theta_Y = 120°$, and the stripes have apparent contact angles $\theta_{a,1} = 150°$ and $\theta_{a,1} = 120°$. As shown in Figure 11a the stripes are oriented along the x-axis and the temperature gradient is either oriented parallel to the stripes or at an angle $\alpha = 45°$. In this figure, we plot the footprint of the 3D droplet along with contours of the temperature field. The greyed areas correspond to $\theta_{a,2} = 120°$ whereas the areas in between have apparent contact angle, $\theta_{a,1} = 150°$. Despite the different direction of the temperature gradient, in both cases we find that droplet moves along the direction of the stripes. This result is in line with the observations of Dai et al.[10] who also found that migration occurred along the grinding scars rather than along the temperature gradient. Similarly, in our case the stripes guide the direction of the droplet migration. When the temperature gradient is not parallel with the stripes, the contact angle hysteresis acts as a barrier preventing migration over the stripes and thus the droplet is driven toward the easier route, i.e., along the stripes.

We also note in Figure 11a that in the case of a 45° angle, the distance that is covered by the droplet at the same time interval

DOI: 10.1021/acs.langmuir.7b02762
Langmuir 2017, 33, 10838−10850

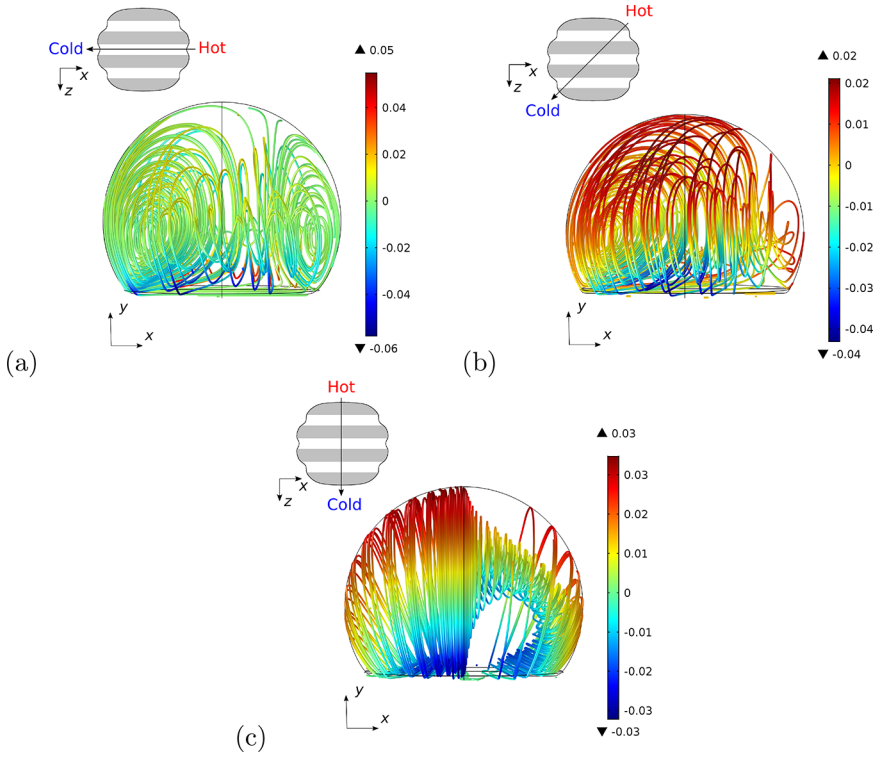

Figure 12. Three-dimensional flow within the drop for a temperature gradient along the solid surface (along the *xz*-plane) that is (a) in parallel (α = 0°), (b) at an angle α = 45°, and (c) vertical (α = 90°) to the direction of the stripes of the solid surface. The stripes are oriented along the *x*-direction and the *z*-direction points toward the reader while the dimensionless wall temperature is given by $T_w = 1 + \Gamma(x \cos \alpha - z \sin \alpha)$. The streamlines have been derived subtracting the migration velocity from the velocity component in the *x*-direction, assuming a system of reference that moves with the droplet, and are colored by the local v_z. The remaining parameters are the same as in Figure 11.

is smaller than in the case of parallel thermal gradient. In Figure 11b we have evaluated the migration velocity of the droplet for different angles of temperature gradient orientation. The symbols depict the results from our 3D calculations and it is clearly shown the maximum migration velocity arises for the parallel case, in direct agreement with Dai et al.[10] In the same figure we have also plotted, with a solid line, a theoretical curve assuming that the migration velocity is given by $U_{\parallel} \cos \alpha$, where $U_{\parallel}$ is the migration velocity for 0°. The agreement is excellent, indicating clearly that the migration velocity is determined only by the active Marangoni stress component in the direction of the stripes. For a vertical temperature gradient (90°) the droplet remains motionless, not being able to overcome the barrier that is set by the contact angle hysteresis. As shown above, by decreasing the contact angle hysteresis or increasing the induced Marangoni stress by imposing a stronger thermal gradient it is possible to overcome this barrier. In Figure 11c, the spatiotemporal evolution of the footprint center is depicted for $\theta_{a,2}$ = 120° and two different values of $\theta_{a,1}$. When the difference between the apparent contact angles is large the droplet moves along the stripes even though the temperature gradient is oriented at 75°. By decreasing this difference, and thus reducing the contact angle hysteresis, the droplet initially moves along the direction of the temperature gradient overcoming one stripe before it eventually starts to follow the easier track along the stripes.

It is also interesting to examine the 3D flow within the drop which is depicted in Figure 12 by means of streamlines colored by the local velocity in the *z*-direction (in the direction toward the reader) for three different orientation of the temperature gradient. For all cases the streamlines have been derived by subtracting the migration velocity from the velocity component in the *x*-direction assuming a system of reference that moves with the droplet. In Figure 12a the gradient is oriented along the *x*-direction (the same direction with the stripes) and the droplet is moving from right to left (toward the colder region). The flow in this case is dominated by the presence of two main vortices along the symmetry plane, a large one in the advancing region of the contact line (cold region) and a smaller one in the receding region (hot region). The nonsymmetric pattern of the flow inside the droplet can be clearly attributed to the directional motion of the droplet along the *x*-direction. As expected the flow in the transverse direction is rather weak except for the regions very close to the solid surface where the temperature gradients are stronger. On the other hand, in Figure 12c the gradient is oriented along the *z*-direction (vertical to the stripes) and the droplet remains motionless. Nevertheless, a strong recirculation vortex arises, covering the entire drop, just like in the case of Figure 7. Flow is driven from part of the contact line that resides on the hot part of the droplet (far side with respect to the reader) to the apex along the interface and to part of the contact line region which is colder (on the reader's side) while the flow is recirculated through the drop core in the direction of the stripes. Finally, the flow in Figure 12b for 45° angle retains characteristics from both limiting cases, i.e., the presence of a vortex in the colder part of the contact line along with a velocity field that also spans in the *z*-direction due to the effect of Marangoni stresses in this direction.

In the discussion of Figure 11 it has been established that both the direction of motion as well as the migration velocity can be significantly affected by the orientation of the structure

DOI: 10.1021/acs.langmuir.7b02762
Langmuir 2017, 33, 10838−10850

with respect to the thermal gradient. One question that arises is whether this effect could be exploited in order to guide a droplet along a predefined track. In the case shown in Figure 13, two superhydrophobic stripes ($\theta_{a,1}$ = 150°) on a smooth hydrophobic surface ($\theta_{a,2} = \theta_Y$ = 120°) define such a track. At t = 0 a droplet is placed inside the track on the hot side. The Marangoni stresses due to the temperature gradient initially accelerate the droplet in the x-direction until it reaches the first corner. At that point, the droplet is unable to overcome the contact angle hysteresis, decelerates, and the velocity rearranges as the droplet eventually makes the turn and accelerates in the z-direction. The droplet under the action of Marangoni stresses and exploiting the contact angle hysteresis of the solid surface is driven through the track and even manages to perform almost a U turn. It is therefore demonstrated that carefully designed structured surfaces can be used in order to passively move droplets along a predefined route.

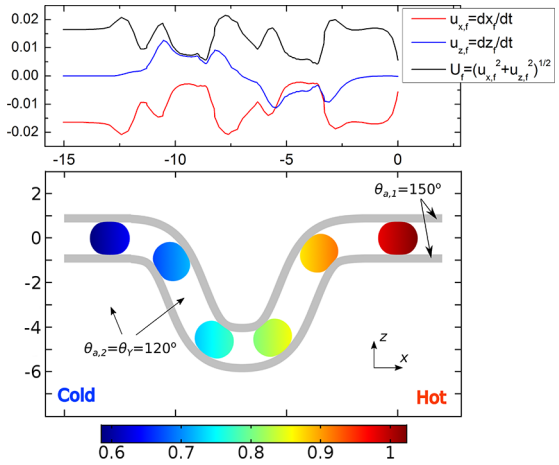

Figure 13. Thermocapillary driven motion along a predefined track. Bottom panel: Footprint of a droplet, along with contours of the local temperature, moving along a track that is defined by two superhydrophobic stripes (shown in gray). Top panel: Migration velocity of the footprint center, U_f, and its components in x- and z-directions. α = 0° and the remaining parameters are the same as in Figure 11.

3.4.2. Droplet Motion through a Narrow Passage. In this section we are interested in a slightly different setup, i.e., a droplet moving through a perforated superhydrophobic defect, and examine under which conditions (thermal gradient, Γ) and hole diameter, D (see Figure 14a) the droplet may pass through or become entrapped by the defect. Such a system would be extremely useful for controlling the droplet motion in microfluidic devices. An obvious application would be to sort droplets, according to their volume, by using a certain hole diameter.

In Figure 14b, we present the mean footprint position of a 3D droplet for different values of Γ for a hole normalized diameter: D/R = 0.85. We observe that, upon reaching the defect, the drop gets trapped for the lower thermal gradient value (Γ = 0.02) as the droplet cannot surpass the contact angle hysteresis. Increasing the thermal gradient (Γ = 0.035), we observe that although the droplet slows down when it reaches the hole (see Figure 14c) the induced Marangoni stresses cause the deformation of the droplet allowing it to eventually pass through the hole, experiencing limited oscillations which soon fade, and these are reflected in the migration velocity (see Figure 14c). For higher values of Γ the droplet becomes even less obstructed by the defect.

In order to determine the critical conditions for the trapping of droplets we have produced a flow map (Figure 15) where we

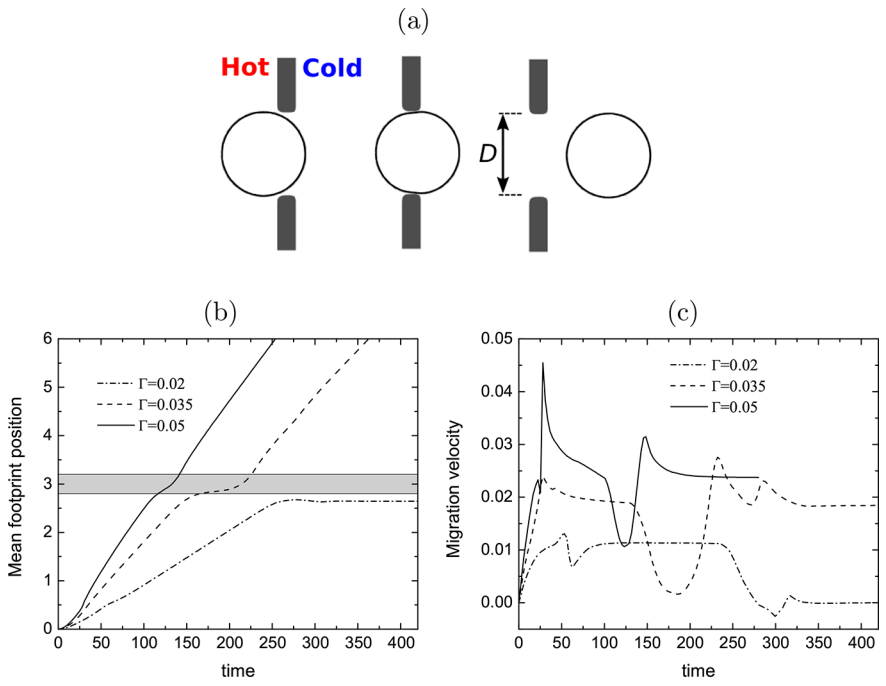

Figure 14. (a) Footprint profiles of a 3D droplet moving on a smooth hydrophobic surface (white area, $\theta_{a,2} = \theta_Y$ = 120°) passing through a perforated superhydrophobic defect (gray area, $\theta_{a,1}$ = 150°) under the influence of a temperature gradient, Γ = 0.04. (b) Temporal evolution of the mean footprint position of the 3D droplet for various thermal gradients. The gray ribbon denotes the position of the superhydrophobic defect. (c) Temporal evolution of the migration velocity of the droplet for different values of Γ. The remaining parameters are Oh = 0.07, Pr = 10, and Ma = 0.5. The hole normalized diameter is D/R = 0.85.

DOI: 10.1021/acs.langmuir.7b02762
Langmuir 2017, 33, 10838−10850

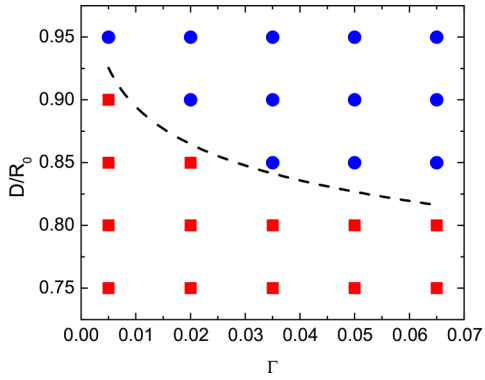

Figure 15. Flow map with cases of a droplet stacking (red squares) or passing (blue circles) through a perforated superdydrophobic defect (see also Figure 14) for various values of the hole normalized diameter, D/R, and Γ. The dashed line delimits the trapped and the passing regions. The remaining parameters are Oh = 0.07, Pr = 10, Ma = 0.5.

vary the driving force (here the thermal gradient, Γ) in the x-axis and the hole normalized diameter, D/R in the y-axis and indicate whether the droplet becomes trapped or passes through the hole. It is interesting here that we recognize a power-law behavior of the trapping limit (the threshold between the stacking and passing cases) (see the dashed line in Figure 15). Similar trends have also been observed in the case of a sliding droplet trapped by a chemical defect[42] or by an electrowetting-induced wettability defect.[43]

4. CONCLUSIONS

We have carried out a numerical investigation of droplet dynamics on nonuniformly heated complex solid surfaces; the droplet is bounded from above by a hydrodynamically passive gas. An efficient sharp-interface model has been employed, which treats the liquid−gas and liquid−solid interfaces in a unified context. The microscale liquid−solid interactions are taken into account through a type of Lennard-Jones potential. The robustness of this scheme is due to the fact that an explicit condition along the contact line is not required and the contact angles emerge naturally as a result of the liquid−solid microscale interactions, capillary pressure, viscous stresses, and thermocapillarity. Crucially, the model has a built-in capability to predict the effect of contact angle hysteresis and in the case of structured solid surfaces it is even possible to predict the effect of static hysteresis for a given substrate structure.

A full parametric study was carried out that focused on the interplay between the effects of the magnitude of the applied temperature gradient, Marangoni stresses, wettability, and geometrical characteristics of the substrate. Our finite element simulations for a 2D droplet indicate that the static hysteresis of the substrate sets a barrier in droplet motion which can be surpassed when the effect of Marangoni stresses becomes strong enough, i.e., beyond a critical value of the applied temperature gradient, in line with experimental observations in the literature. Droplet migration is also impeded by decreasing wettability of the solid surface. We show that in the case of an ambient gas with negligible viscosity the critical contact angle for motionless state in the absence of static hysteresis, i.e., for a smooth solid surface, is predicted at ≈165°; this result is in contrast to the previous study by Sui[21] which predicted an asymptote ≈100° with decreasing viscosity ratios using the level-set method. Clearly the combined effect of static hysteresis and decreasing wettability can lead to lower values of critical angle for a motionless state. We also show that when the droplet is in a motionless state, Marangoni stresses drive a recirculating flow inside the droplet which could be exploited to enhance mixing, e.g., in the case of a microreactor. The mixing time is in fact found to be comparable with other methods such as electrowetting-induced droplet oscillations.[37,38]

Since in realistic applications the three-dimensional characteristics of the flow can also be important, we have also performed 3D simulations. We have focused on the case of hydrophobic surfaces and examined the effect of the temperature gradient orientation with respect to that of the stripes as well as the droplet motion through a wetting defect. It is shown that the barrier due to the static hysteresis plays a determining role in the resulting droplet migration path by forcing the droplet move along the easiest path such as the direction of specific geometrical characteristics of the substrate, e.g., stripes. We show that this can exploited in order to passively control the direction of droplet motion.

As a last note, we would like to mention that, for the purposes of the present study, the effect of evaporation has been neglected by assuming that the droplet is nonvolatile. However, in realistic applications it is expected that evaporation may come into play, provided that the temperature of operation is sufficiently high or the application of thermal gradients has to be extended for very long times. The presence of evaporation, besides the loss of the liquid due to vaporization, may also affect the temperature field along the liquid−air interface, due to the latent heat of evaporation, thus affecting the induced Marangoni stresses and in turn the flow inside the droplet as well as the droplet motion. We believe that future studies should also make an attempt to take this effect into account in our way to provide a better understanding of the various factors that affect thermocapillary droplet actuation.

■ ASSOCIATED CONTENT

Supporting Information

The Supporting Information is available free of charge on the ACS Publications website at DOI: 10.1021/acs.langmuir.7b02762.

Movie S1: Animation of the droplet footprint for a temperature gradient at an angle α = 75° with hydrophobic stripes of $\theta_{a,1}$ = 130° and $\theta_{a,2}$ = θ_Y = 120°, for Oh = 0.07, Pr = 10, Ma = 0.5, Γ = 0.05 (AVI)

■ AUTHOR INFORMATION

Corresponding Author

*E-mail: pathan@chemeng.ntua.gr.

ORCID

Nikolaos T. Chamakos: 0000-0002-6644-3600

Athanasios G. Papathanasiou: 0000-0002-8468-8126

Notes

The authors declare no competing financial interest.

■ ACKNOWLEDGMENTS

The authors kindly acknowledge funding from the European Research Council under the Europeans Communitys Seventh Framework Programme (FP7/2007-2013)/ERC grant agreement no. [240710].

DOI: 10.1021/acs.langmuir.7b02762
Langmuir 2017, 33, 10838−10850

REFERENCES

(1) Stone, H. A.; Stroock, A. D.; Ajdari, A. Engineering flows in small devices: Microfluidics toward a lab-on-a-chip. *Annu. Rev. Fluid Mech.* **2004**, *36*, 381−411.
(2) Darhuber, A. A.; Troian, S. M. Principles of microfluidic actuation by modulation of surface stresses. *Annu. Rev. Fluid Mech.* **2005**, *37*, 425−455.
(3) Whitesides, G. M. The origins and the future of microfluidics,. *Nature* **2006**, *442*, 368−373.
(4) Karbalaei, A.; Kumar, R.; Cho, H. J. Thermocapillarity in microfluidics - a review. *Micromachines* **2016**, *7*, 13.
(5) Bouasse, H. *Capillarite: phenomenes superficiels*; Librairie Delgrave: Paris, 1924.
(6) Yarin, A. L.; Liu, W.; Reneker, D. H. Motion of droplets along thin fibers with temperature gradient. *J. Appl. Phys.* **2002**, *91*, 4751−4760.
(7) Brzoska, J. B.; Brochard-Wyart, F.; Rondelez, F. Motions of droplets on hydrophobic model surfaces induced by thermal gradients. *Langmuir* **1993**, *9* (8), 2220−2224.
(8) Chen, J. Z.; Troian, S. M.; Darhuber, A. A.; Wagner, S. Effect of contact angle hysteresis on thermocapillary droplet actuation. *J. Appl. Phys.* **2005**, *97* (1), 014906.
(9) Pratap, V.; Moumen, N.; Subramanian, R. S. Thermocapillary motion of a liquid drop on a horizontal solid surface. *Langmuir* **2008**, *24* (9), 5185−5193.
(10) Dai, Q.; Huang, W.; Wang, X. Surface roughness and orientation effects on the thermo-capillary migration of a droplet of paraffin oil. *Exp. Therm. Fluid Sci.* **2014**, *57*, 200−206.
(11) Karapetsas, G.; Sahu, K. C.; Matar, O. K. Effect of contact line dynamics on the thermocapillary motion of a droplet on an inclined plate. *Langmuir* **2013**, *29* (28), 8892−8906.
(12) Brochard, F. Motions of droplets on solid surfaces induced by chemical or thermal gradients. *Langmuir* **1989**, *5* (2), 432−438.
(13) Ford, M. L.; Nadim, A. Thermocapillary migration of an attached drop on a solid surface. *Phys. Fluids* **1994**, *6* (9), 3183−3185.
(14) Smith, M. K. Thermocapillary migration of a two-dimensional liquid droplet on a solid surface. *J. Fluid Mech.* **1995**, *294*, 209.
(15) Gomba, J. M.; Homsy, G. M. Regimes of thermocapillary migration of droplets under partial wetting conditions. *J. Fluid Mech.* **2010**, *647*, 125.
(16) Karapetsas, G.; Sahu, K. C.; Sefiane, K.; Matar, O. K. Thermocapillary-driven motion of a sessile drop: Effect of non-monotonic dependence of surface tension on temperature. *Langmuir* **2014**, *30*, 4310−4321.
(17) Ehrhard, P.; Davis, S. H. Non-isothermal spreading of liquid drops on horizontal plates. *J. Fluid Mech.* **1991**, *229*, 365−388.
(18) Anderson, D. M.; Davis, S. H. The spreading of volatile liquid droplets on heated surfaces. *Phys. Fluids* **1995**, *7* (2), 248.
(19) Karapetsas, G.; Matar, O. K.; Valluri, P.; Sefiane, K. Convective rolls and hydrothermal waves in evaporating sessile drops. *Langmuir* **2012**, *28*, 11433−11439.
(20) Chen, J.-C.; Kuo, C.-W.; Neitzel, G. Numerical simulation of thermocapillary nonwetting. *Int. J. Heat Mass Transfer* **2006**, *49*, 4567−4576.
(21) Sui, Y. Moving towards the cold region or the hot region? Thermocapillary migration of a droplet attached on a horizontal substrate. *Phys. Fluids* **2014**, *26* (9), 092102.
(22) Tseng, Y.-T.; Tseng, F.-G.; Chen, Y.-F.; Chieng, C.-C. Fundamental studies on micro-droplet movement by marangoni and capillary effects. *Sens. Actuators, A* **2004**, *114* (2), 292−301.
(23) Nguyen, H.-B.; Chen, J.-C. A numerical study of thermocapillary migration of a small liquid droplet on a horizontal solid surface,. *Phys. Fluids* **2010**, *22*, 062102.
(24) Fath, A.; Bothe, D. Direct numerical simulations of thermocapillary migration of a droplet attached to a solid wall. *Int. J. Multiphase Flow* **2015**, *77*, 209−221.
(25) Pradhan, T. K.; Panigrahi, P. K. Thermocapillary convection inside a stationary sessile water droplet on a horizontal surface with an imposed temperature gradient. *Exp. Fluids* **2015**, *56*, 178.
(26) Chamakos, N. T.; Kavousanakis, M. E.; Papathanasiou, A. G. Enabling efficient energy barrier computations of wetting transitions on geometrically patterned surfaces. *Soft Matter* **2013**, *9* (40), 9624.
(27) Chamakos, N. T.; Kavousanakis, M. E.; Papathanasiou, A. G. Neither Lippmann nor Young: Enabling Electrowetting Modeling on Structured Dielectric Surfaces. *Langmuir* **2014**, *30* (16), 4662−4670.
(28) Chamakos, N. T.; Kavousanakis, M. E.; Boudouvis, A. G.; Papathanasiou, A. G. Droplet spreading on rough surfaces: Tackling the contact line boundary condition. *Phys. Fluids* **2016**, *28* (2), 022105.
(29) Karapetsas, G.; Chamakos, N. T.; Papathanasiou, A. G. Efficient modelling of droplet dynamics on complex surfaces. *J. Phys.: Condens. Matter* **2016**, *28* (8), 085101.
(30) Tucker, P. Differential equation-based wall distance computation for DES and RANS. *J. Comput. Phys.* **2003**, *190* (1), 229−248.
(31) Koplik, J.; Banavar, J. R.; Willemsen, J. F. Molecular dynamics of fluid flow at solid surfaces. *Phys. Fluids A* **1989**, *1* (5), 781−794.
(32) Barthlott, W.; Neinhuis, C. Purity of the sacred lotus, or escape from contamination in biological surfaces. *Planta* **1997**, *202* (1), 1−8.
(33) Tam, D.; von Arnim, V.; McKinley, G.; Hosoi, A. Marangoni convection in droplets on superhydrophobic surfaces. *J. Fluid Mech.* **2009**, *624*, 101−123.
(34) Davanlou, A.; Kumar, R. Passive mixing enhancement of microliter droplets in a thermocapillary environment. *Microfluid. Nanofluid.* **2015**, *19*, 1507−1513.
(35) Squires, T. M.; Quake, S. R. Microfluidics: Fluid physics at the nanoliter scale. *Rev. Mod. Phys.* **2005**, *77* (3), 977.
(36) Samiei, E.; Tabrizian, M.; Hoorfar, M. A review of digital microfluidics as portable platforms for lab-on a-chip applications. *Lab Chip* **2016**, *16* (13), 2376−2396.
(37) Mugele, F.; Baret, J.-C.; Steinhauser, D. Microfluidic mixing through electrowetting-induced droplet oscillations. *Appl. Phys. Lett.* **2006**, *88* (20), 204106.
(38) Mugele, F.; Staicu, A.; Bakker, R.; van den Ende, D. Capillary stokes drift: a new driving mechanism for mixing in ac-electrowetting. *Lab Chip* **2011**, *11* (12), 2011.
(39) Stroock, A. D.; Dertinger, S. K.; Ajdari, A.; Mezić, I.; Stone, H. A.; Whitesides, G. M. Chaotic mixer for microchannels. *Science* **2002**, *295* (5555), 647−651.
(40) Muradoglu, M.; Stone, H. A. Mixing in a drop moving through a serpentine channel: A computational study. *Phys. Fluids* **2005**, *17* (7), 073305.
(41) Ottino, J. *The Kinematics of Mixing: Stretching, Chaos, and Transport, Cambridge Texts in Applied Mathematics*; Cambridge University Press, 1989.
(42) Cavalli, A.; Musterd, M.; Mugele, F. Numerical investigation of dynamic effects for sliding drops on wetting defects. *Phys. Rev. E* **2015**, *91* (2), 023013.
(43) Mannetje, D.; Ghosh, S.; Lagraauw, R.; Otten, S.; Pit, A.; Berendsen, C.; Zeegers, J.; Van Den Ende, D.; Mugele, F. Trapping of drops by wetting defects. *Nat. Commun.* **2014**, *5*, 3559.

DOI: 10.1021/acs.langmuir.7b02762
Langmuir 2017, 33, 10838−10850